

Mass and energy balance calculations for artificial ice reservoirs (Icestupas)

Suryanarayanan Balasubramanian^{1*}, Martin Hoelzle¹, Michael Lehning²,
Sonam Wangchuk³, Johannes Oerlemans⁴, Felix Keller^{5,6} and Jordi Bolíbar⁴

¹ University of Fribourg, Fribourg, Switzerland

² WSL Institute for Snow and Avalanche Research, Davos, Switzerland

³ Himalayan Institute of Alternatives Ladakh, Leh, India

⁴ Institute for Marine and Atmospheric Research, Utrecht University, Utrecht, The Netherlands

⁵ Academia Engiadina, Samedan, Switzerland

⁶ ETH, Zürich, Switzerland

Correspondence*:

Suryanarayanan Balasubramanian

suryanarayanan.balasubramanian@unifr.ch

2 ABSTRACT

Artificial Ice Reservoirs (AIRs) can successfully store water during winter and release the water during spring and summer. This makes them a reliable fresh water resource for irrigation in dry environments. Several AIRs have been built but studies of their water storage capacity and efficiency are scarce. This study models a cone-shaped AIR popularly called Icestupa. Processes involved in the development and temporal evolution of an Icestupa are calculated by a physically-based model using equations governing the heat transfer, vapour diffusion and transport of water that undergoes phase changes. These processes were quantified using meteorological data in conjunction with fountain spray information (mass input of an AIR) to estimate the quantity of frozen, melted, evaporated and runoff water for three sites in Switzerland and one in India. At these measurement sites, AIR were built for model validation purposes. The model was further tested by performing a sensitivity and uncertainty study showing that the most sensitive parameters are the ice emissivity and the temperature threshold used to determine precipitation phase. Model calculations estimate that the AIR stored about % of the total water sprayed as ice.

Keywords: icesuppa, mass balance, water storage, climate change adaptation, geoengineering

1 INTRODUCTION

Seasonal snow cover, glaciers and permafrost are expected to change their water storage capacity due to climate change with major consequences for downriver water supply (Immerzeel et al., 2019). The challenges brought about by these changes are especially important for dry mountain environments such as in Central Asia or the Andes, which directly rely on the seasonal meltwater for their farming and drinking needs (Hoelzle et al., 2019; Apel et al., 2018; Buytaert et al., 2017; Chen et al., 2016; Unger-Shayesteh et al., 2013). Some villages in Ladakh, India have already been forced to relocate due to glacial retreat and the corresponding loss of their main fresh water resources (Grossman, 2015).



Figure 1. Icestupa in Ladakh, India on March 2017 was 24 m tall and contained around 3700 m³ of water.
Picture Credits: Lobzang Dadul

24 Artificial ice reservoirs (AIRs) have been considered to be a feasible way to adapt to these changes (Hock
25 et al., 2019; Nüsser et al., 2019b). An AIR is a human-made ice structure typically constructed during the
26 cold winter months and designed to slowly release freshwater during the warm and dry spring and summer
27 months. The main purpose of AIRs is irrigation. Therefore, AIRs are designed to store water in the form of
28 ice as long into the summer as possible. The energy required to construct an AIR is usually derived from
29 the gravitational head of the source water body. Some are constructed horizontally by freezing water using
30 a series of checkdams and others are built vertically by spraying water through fountain systems (Nüsser
31 et al., 2019a). The latter are colloquially referred to as Icestupas and are the subject of this study.

32 A typical Icestupa just requires a pipeline attached to a vertically mounted metal pipe with a fountain
33 nozzle for construction. Their water source is usually a high altitude lake or glacial stream. Due to the
34 altitude difference between the pipeline input and fountain output, water ejects from the fountain nozzle as
35 droplets that eventually lose their latent heat to the atmosphere and accumulate as ice around the metal pipe.
36 The fountain nozzle is raised through addition of further pipes as and when significant ice accumulates.
37 Typically, a dome of branches is constructed around the metal pipe so that such pipe extensions can be
38 done from within this dome. During the winter, the fountain is manually activated from sunset to sunrise.
39 Threads, tree branches and fishing nets are used to guide and accelerate the ice formation.

40 Since their invention in 2013 (Wangchuk, 2014), Icestupas have gained widespread publicity in the region
41 of Ladakh, Northern India since they require very little infrastructure, skills and energy to be constructed
42 in comparison to other water storage technologies. Compared to other AIR geometries, Icestupas (Fig.
43 1) can be built at lower altitudes and last much longer into the summer than other types of ice structures
44 (Wangchuk, 2014). However, to date, no reliable estimates exist about the amount of sprayed water that
45 is necessary to create them and the meltwater they provide (Nüsser et al., 2019a). Rough estimates of
46 Icestupa meltwater in Ladakh suggest that the water loss during the construction process is considerable
47 (see Appendix 8.1). A complete set of measurements of the water storage and energy balance are required
48 to understand the cause of the water losses better and increase the construction efficiency.

49 In this paper, we aim to develop a physically-based model of a vertical AIR (or Icestupa) that can quantify
50 their storage efficiency using existing weather and water usage information. Mass and energy balance

Table 1. The Scientific AIR

AIR	Gangles, 2021	Guttannen, 2021	Guttannen, 2020	Schwarzsee, 2019
Code	IN21	CH21	CH20	CH19
Altitude [m a.s.l.]	4025	1047	1047	967
Fountain Duration	Jan 18 - Mar 10	Nov 22 - Feb 21	Jan 3 - Feb 27	Jan 30 - Feb 16
Drone Flights	6	9	3	0
r_{spray} [m]	10.8	6.9	7.7	1.2
V_{dome} [m ³]	78.5	13.2	23.9	0

equations were used to estimate the quantity of water frozen, melted, evaporated and runoff. Sensitivity and uncertainty analysis were performed to identify the most critical parameters and the variance caused by them. For validation, we chose four AIR built across the winters of 2019, 2020 and 2021 in India and Switzerland. Our model and validation experiments provide first steps towards evaluating the effectiveness of a vertical AIR for irrigation and allow us to outline some preliminary guidelines for consideration when a construction of an Icestupa for water storage is envisaged.

2 STUDY SITES

To accurately estimate and validate the ice volume of AIR the model requires three kinds of datasets namely, weather, water and ice volume. So through the winters of 2019, 2020 and 2021 several scientific AIR were constructed by teams in Switzerland and India. Each site had an Automatic Weather Station (AWS) nearby. Also drone flights were conducted periodically to record AIR ice volume. The model was applied on four of the AIR which have a relatively complete dataset associated with them as shown in Table 1. For brevity, only the model application on CH21 AIR is discussed below.

2.1 CH21 AIR

The Guttannen (CH21) site in the Bern region lies at 1047 m a.s.l.. In the winter (Oct-Apr), mean daily minimum and maximum air temperatures vary between -13 and 15 °C. Clear skies are rare, averaging around 7 days during winter (Meteoblue, 2020). The site was situated adjacent to a stream resulting in high humidity values across the study period as shown in Fig. 2. The fountain used for spraying water had an initial height of 2.3 m. The water was transferred from a spring water source and flowed via a flowmeter to the nozzle. In addition, a webcam guaranteed a continuous survey of the site during the construction of the AIR.

The CH21 AIR was constructed by Guttannen Bewegt Association on a garden adjacent to a stream in Guttannen, Switzerland. To initiate the ice formation process, tree branches were laid covering the fountain pipe. The fountain height varied between 2 to 5 m during the construction period. Fountain operation was guided by temperature conditions.

2.1.1 Weather measurements

Air temperature, relative humidity, wind speed, pressure, longwave, shortwave direct and diffuse radiation are required to calculate the surface energy balance of an AIR. For the CH21 AIR, the weather data was primarily drawn from a meteoswiss AWS located 184 m away from the construction site. In addition, we used ERA5 reanalysis dataset (Copernicus Climate Change Service (C3S), 2017) for filling data gaps and adding data that were not measured directly as shown in Fig. 3. Zero wind speed values were recorded whenever snow accumulated on the ultrasonic wind sensor. It was assumed this was the cause when null



Figure 2. Bird's eye view of the CH21 AIR

82 wind speeds were observed continuously for atleast 3 hours. All such null values were replaced using the
83 ERA5 dataset.

84 The ERA5 reanalysis dataset has a good correlation with lower elevation sites in Switzerland (Scherrer,
85 2020). The ERA5 grid point chosen (Latitude 46° 38' 24" N, Longitude 8° 15' 00" E) for the CH21 site was
86 around 3.6 km away from the actual site. All the ERA5 variables were therefore fitted with the meteoswiss
87 dataset via linear regressions.

88 2.1.2 Discharge measurements

89 The water flow rate or discharge was measured via an ultrasonic sensor attached to the fountain supply
90 pipeline. However, due to various malfunctions, the discharge measurements were very sparse and could not
91 be extrapolated for the complete measurement period. Instead the discharge duration was first determined
92 using the hourly webcam images of the CH21 site. The available discharge measurement was later used to
93 determine the average discharge quantity (10 l/min) during these periods.

94 2.1.3 Ice volume measurements

95 Several Drone flights were conducted in every AIR site. The DEM generated through these flights were
96 analysed to obtain the circumference and volume of the ice structure. The mean circumference measured
97 during the fountain duration was set as the spray radius (r_{spray}) and the first drone flight was used to set
98 the dome volume (V_{dome}) for model initialisation. The ice volume data was later used for calibration and
99 validation of the model.

100 The model application is restricted to CH21 AIR below. Model results and figures for other AIR can be
101 found in the supplementary materials.

3 MODEL SETUP

102 A bulk energy and mass balance model is used to calculate the amounts of ice, meltwater, water vapour
103 and runoff water of the AIR every hour. This model consists of four modules which estimates the AIR, a)
104 geometric evolution , b) energy balance, c) surface temperature and d) mass balance.

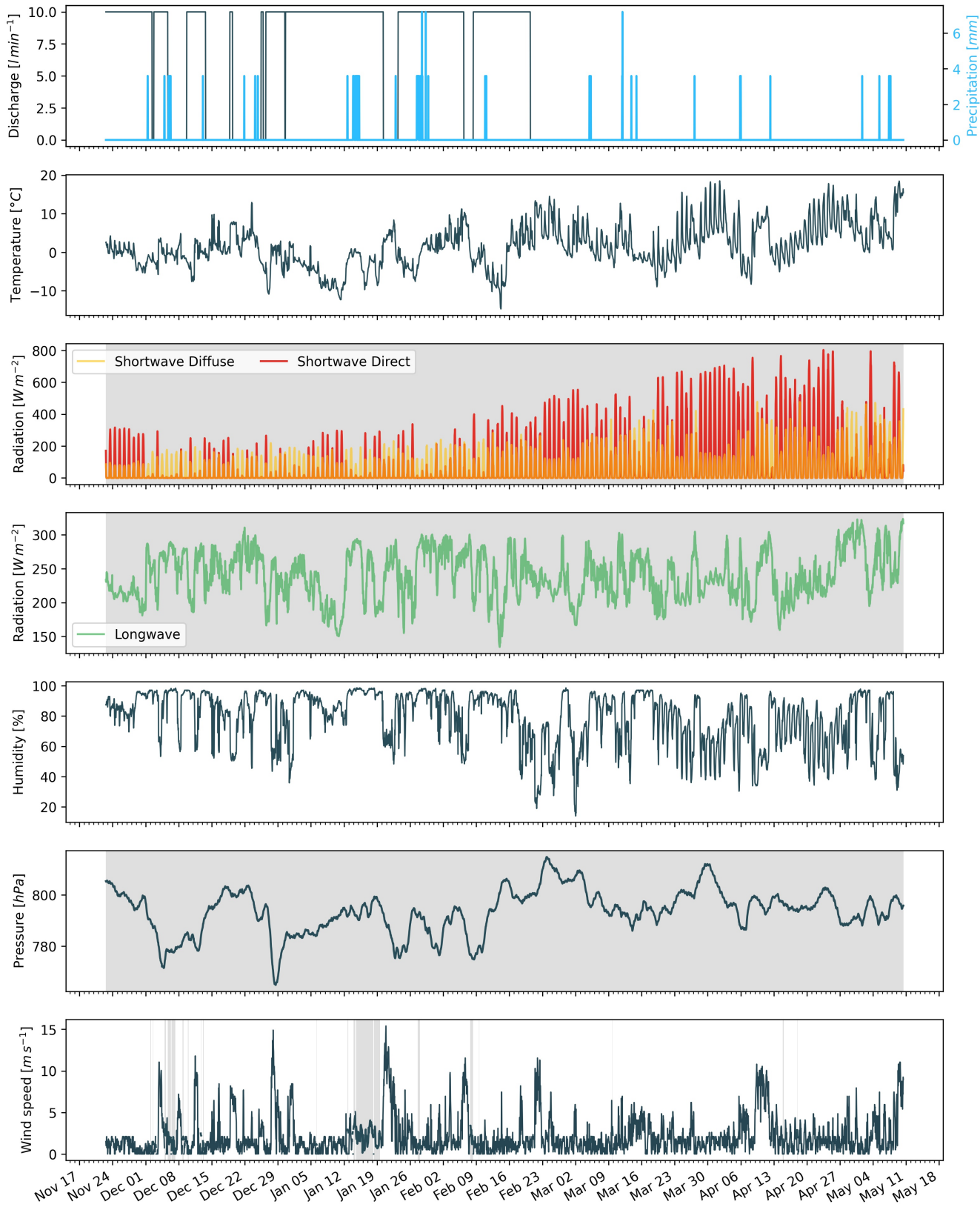


Figure 3. Measurements at the AWS of CH21 were used as main model input data in hourly frequency. Missing data, data gaps and errors were filled from the ERA5 dataset (shaded regions).

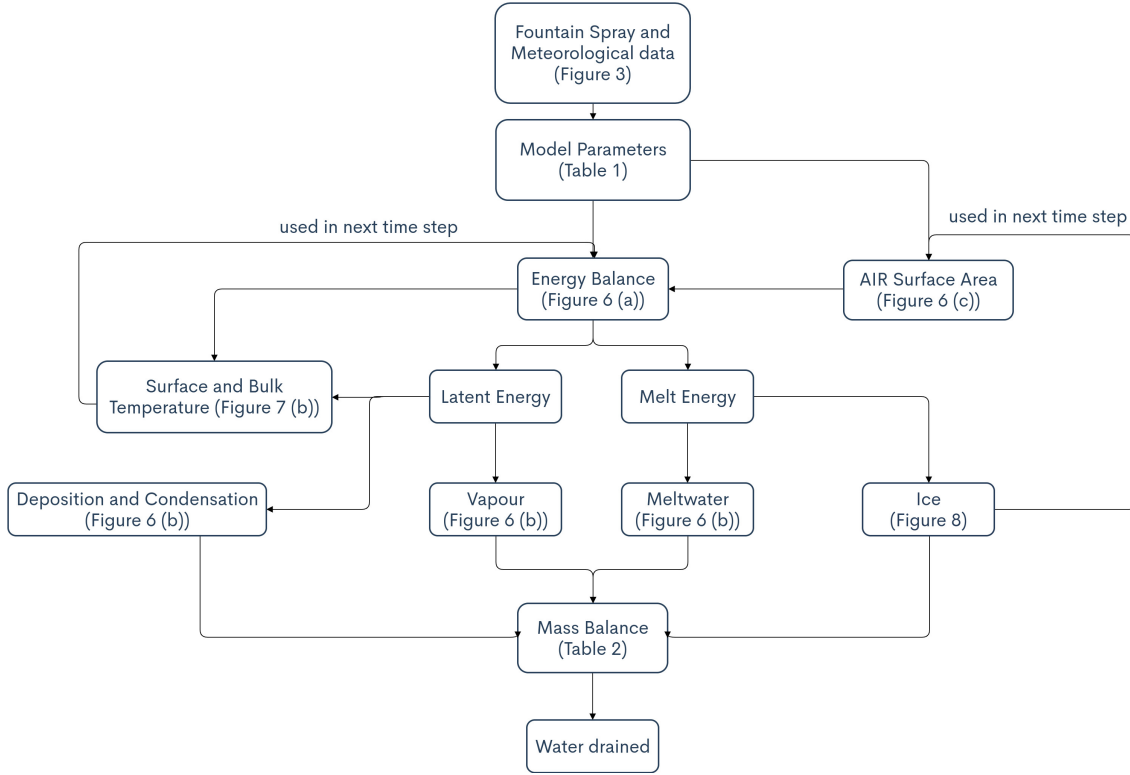


Figure 4. Model schematic showing the algorithm used in the model at every time step. Further details about the variables can be found in the associated tables and figures.

105 3.1 Geometric evolution

106 Radius r_{ice}^i and height h_{ice}^i define the dimensions of the AIR assuming its geometry to be a cone. The
107 surface area A^i exposed to the atmosphere and volume V^i are:

$$A = \pi \cdot r_{ice} \cdot \sqrt{r_{ice}^2 + h_{ice}^2} \quad (1)$$

$$V = \pi/3 \cdot r_{ice}^2 \cdot h_{ice} \quad (2)$$

108 Note that we do not specify the time step superscript i of the shape variables A , V , r_{ice} and h_{ice} for
109 brevity. The equations used henceforth display model time step superscript i only if it is different from the
110 current time step.

111 With the mass of the AIR M_{ice} , its current volume can also be expressed as:

$$V = M_{ice}/\rho_{ice} \quad (3)$$

112 where ρ_{ice} is the density of ice (917 kg m^{-3}).

113 The influence of the AIR fountain is parameterised by the fountain water temperature T_w and its spray
114 radius r_{spray} . The initial radius r_0 of the AIR is assumed to be r_{spray} . The initial height h_0 depends on the
115 dome volume V_{dome} used to construct the AIR as follows:

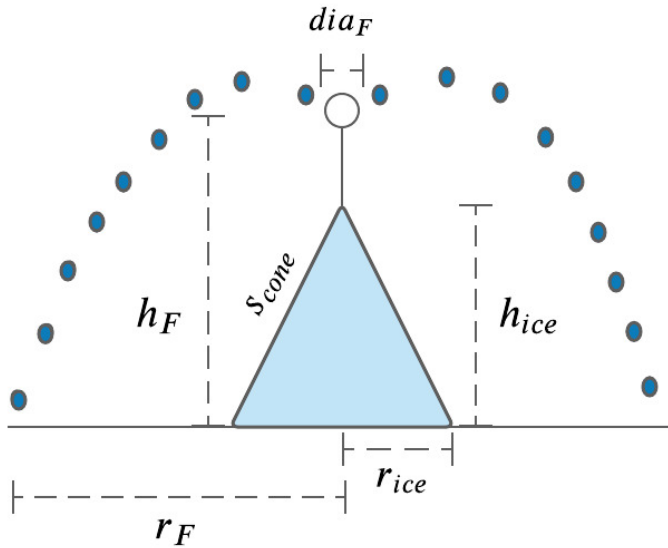


Figure 5. Shape variables and fountain constants of the CH21 Icestupa. r_{ice} is the radius, h_{ice} is the height and s_{cone} is the slope of the ice cone. r_{spray} is the spray radius, h_F is the height and dia_F is the nozzle diameter of the fountain.

$$h_0 = \Delta x + \frac{3 \cdot V_{dome}}{\pi r_{spray}^2} \quad (4)$$

116 where Δx is the surface layer thickness (defined in Section 3.2)

117 During subsequent time steps, the dimensions of the AIR evolve assuming a uniform ice formation and
118 decay across its surface area with an invariant slope $s_{cone} = \frac{h_{ice}}{r_{ice}}$. During these time steps, the volume is
119 parameterised using Eqn. 2 as:

$$V = \frac{\pi \cdot r_{ice}^3 \cdot s_{cone}}{3} \quad (5)$$

120 However, the Icestupa cannot outgrow the maximum range of the water droplets ($(r_{ice})_{max} = r_F$).
121 Combining equations 2, 4, 3 and 5, the geometric evolution of the Icestupa at each time step i can be
122 determined by considering the following rules:

$$(r_{ice}, h_{ice}) = \begin{cases} (r_{spray}, h_0) & \text{if } i = 0 \\ (r_{ice}^{i-1}, \frac{3 \cdot M_{ice}}{\pi \cdot \rho_{ice} \cdot (r_{ice}^{i-1})^2}) & \text{if } r_{ice}^{i-1} \geq r_F \text{ and } \Delta M_{ice} > 0 \\ (\frac{3 \cdot M_{ice}}{\pi \cdot \rho_{ice} \cdot s_{cone}})^{1/3} \cdot (1, s_{cone}) & \text{otherwise} \end{cases} \quad (6)$$

123 where $\Delta M_{ice} = M_{ice}^{i-1} - M_{ice}^{i-2}$

124 3.2 Energy Balance

125 The energy balance equation (Hock, 2005) for the AIR is formulated as follows:

$$q_{SW} + q_{LW} + q_L + q_S + q_F + q_G = q_{surf} \quad (7)$$

126 where q_{surf} is the surface energy flux in [$W\ m^{-2}$]; q_{SW} is the net shortwave radiation; q_{LW} is the net
 127 longwave radiation; q_L and q_S are the turbulent latent and sensible heat fluxes. q_F represents the heat
 128 exchange of the fountain water droplets with the AIR ice surface. q_G represents ground heat flux between
 129 Icestupa surface and Icestupa interior. Energy transferred in the direction of the ice surface is always
 130 denoted as positive and away as negative.

131 Equation 7 is usually referred to as the energy budget for “the surface”, but practically it must apply
 132 to a surface layer of ice with a finite thickness Δx . The energy flux acts upon the Icestupa surface layer
 133 which has an upper and a lower boundary defined by the atmosphere and the ice body of the Icestupa,
 134 respectively. The parameter selection for Δx is based on the following two arguments: (a) the ice thickness
 135 Δx should be small enough to represent the surface temperature variations every model time step Δt and
 136 (b) Δx should be large enough for these temperature variations to not reach the bottom of the surface layer.
 137 Therefore, we introduced a 20 mm thick surface layer for a model time step of 1 hour, over which the
 138 energy balance is calculated. A sensitivity analysis was later performed to understand the influence of this
 139 factor. Here, we define the surface temperature T_{ice} to be the modelled average temperature of the Icestupa
 140 surface layer and the energy flux q_{surf} is assumed to act uniformly across the Icestupa area A .

141 3.2.1 Net Shortwave Radiation q_{SW}

142 The net shortwave radiation q_{SW} is computed as follows:

$$q_{SW} = (1 - \alpha) \cdot (SW_{direct} \cdot f_{cone} + SW_{diffuse}) \quad (8)$$

143 where SW_{direct} and $SW_{diffuse}$ are the ERA5 direct and diffuse short wave radiation, α is the modelled
 144 albedo and f_{cone} is the area fraction of the ice structure exposed to the direct shortwave radiation.

145 We model the albedo using a scheme described in Oerlemans and Knap (1998). The scheme records the
 146 decay of albedo with time after fresh snow is deposited on the surface. δt records the number of time steps
 147 after the last snowfall event. After snowfall, albedo changes over a time step, δt , as

$$\alpha = \alpha_{ice} + (\alpha_{snow} - \alpha_{ice}) \cdot e^{(-\delta t)/\tau} \quad (9)$$

148 where α_{ice} is the bare ice albedo value (0.35), α_{snow} is the snow ice albedo value (0.85) and τ is a decay
 149 rate, which determines how fast the albedo of the ageing snow reaches this value. The decay rate τ is
 150 assumed to have a base value of 10 days similar to values obtained by Schmidt et al. (2017) for wet surfaces
 151 and its maximal value is set based on observations by Oerlemans and Knap (1998) as shown in Table 2.
 152 Furthermore, the albedo α varies depending on the water source that formed the current Icestupa surface.
 153 Correspondingly, the albedo is reset to the value of bare ice albedo if the fountain is spraying water onto
 154 the current ice surface and to the value of fresh snow albedo if a snowfall event occurred. Snowfall events
 155 are assumed if the air temperature is below $T_{ppt} = 1^{\circ}C$ (Fujita and Ageta, 2000).

156 The area fraction f_{cone} of the ice structure exposed to the direct shortwave radiation depends on the
 157 shape considered. The direct solar radiation incident on the AIR surface is first decomposed into horizontal
 158 and vertical components using the solar elevation angle θ_{sun} . For a conical shape, half of the total curved
 159 surface is exposed to the vertical component of the direct shortwave radiation and the projected triangle
 160 of the curved surface is exposed to the horizontal component of the direct shortwave radiation. The solar
 161 elevation angle θ_{sun} used is modelled using the parametrisation proposed by Woolf (1968). Accordingly,
 162 f_{cone} is determined as follows:

$$f_{cone} = \frac{(0.5 \cdot r_{ice} \cdot h_{ice}) \cdot \cos\theta_{sun} + (\pi \cdot r_{ice}^2 / 2) \cdot \sin\theta_{sun}}{\pi \cdot r_{ice} \cdot (r_{ice}^2 + h_{ice}^2)^{1/2}} \quad (10)$$

163 The ERA5 diffuse shortwave radiation is assumed to impact the conical Icestupa surface uniformly.

164 3.2.2 Net Longwave Radiation q_{LW}

165 The net longwave radiation q_{LW} is determined as follows:

$$q_{LW} = LW_{in} - \sigma \cdot \epsilon_{ice} \cdot (T_{ice} + 273.15)^4 \quad (11)$$

166 where T_a represents the measured air temperature, T_{ice} is the modelled surface temperature, both
167 temperatures are given in $^{\circ}\text{C}$, $\sigma = 5.67 \cdot 10^{-8} \text{ J m}^{-2} \text{ s}^{-1} \text{ K}^{-4}$ is the Stefan-Boltzmann constant, LW_{in}
168 denotes the incoming longwave radiation derived from the ERA5 dataset and ϵ_{ice} is the corresponding
169 emissivity value for the Icestupa surface (see Table 2).

170 3.2.3 Turbulent sensible q_S and latent q_L heat fluxes

171 The turbulent sensible q_S and latent heat q_L fluxes are computed with the following expressions proposed
172 by Garratt (1992):

$$q_S = c_a \cdot \rho_a \cdot p_a / p_{0,a} \cdot \frac{\kappa^2 \cdot v_a \cdot (T_a - T_{ice})}{(\ln \frac{h_{AWS}}{z_{ice}})^2} \quad (12)$$

$$q_L = 0.623 \cdot L_s \cdot \rho_a / p_{0,a} \cdot \frac{\kappa^2 \cdot v_a (p_{v,a} - p_{v,ice})}{(\ln \frac{h_{AWS}}{z_{ice}})^2} \quad (13)$$

173 where h_{AWS} is the measurement height above the ground surface of the AWS (in m), v_a is the wind
174 speed in $[m s^{-1}]$, c_a is the specific heat of air at constant pressure ($1010 \text{ J kg}^{-1} \text{ K}^{-1}$), ρ_a is the air density
175 at standard sea level (1.29 kg m^{-3}), $p_{0,a}$ is the air pressure at standard sea level (1013 hPa), κ is the
176 von Karman constant (0.4), L_s is the heat of sublimation (2848 kJ kg^{-1}) and z_{ice} (1.7 mm) denotes the
177 roughness length of ice (momentum and scalar). The vapor pressures over air ($p_{v,a}$) and ice ($p_{v,ice}$) was
178 obtained using the following formulation given in WMO (2018):

$$p_{v,a} = 6.107 \cdot 10^{(7.5 \cdot T_a / (T_a + 237.3))} \\ p_{v,ice} = (1.0016 + 3.15 \cdot 10^{-6} \cdot p_a - 0.074 \cdot p_a^{-1}) \cdot (6.112 \cdot e^{(22.46 \cdot T_{ice} / (T_{ice} + 272.62))}) \quad (14)$$

179 where p_a is the measured air pressure in [hPa].

180 3.2.4 Fountain water heat flux q_F

181 The interaction between the fountain water and the ice surface is taken into account by assuming that
182 the ice surface temperature remains constant at 0°C during time steps when the fountain is active. This
183 process can be divided into two simultaneous steps: (a) the water temperature T_{water} is cooled to 0°C
184 and (b) the ice surface temperature is warmed to 0°C . Thus, the heat flux caused by the fountain water is
185 calculated as follows:

$$q_F = \begin{cases} 0 & \text{if } \Delta M_F = 0 \\ \frac{\Delta M_F \cdot c_{water} \cdot T_{water}}{\Delta t \cdot A} + \frac{\rho_{ice} \cdot \Delta x \cdot c_{ice} \cdot T_{ice}}{\Delta t} & \text{if } \Delta M_F > 0 \end{cases} \quad (15)$$

186 with c_{ice} as the specific heat of ice.

187 3.2.5 Bulk Icestupa heat flux q_G

188 The bulk Icestupa heat flux q_G corresponds to the ground heat flux in normal soils and is caused by the
 189 temperature gradient between the surface layer (T_{ice}) and the ice body (T_{bulk}). It is expressed by using the
 190 heat conduction equation as follows:

$$q_G = k_{ice} \cdot (T_{bulk} - T_{ice}) / l_{ice} \quad (16)$$

191 where k_{ice} is the thermal conductivity of ice ($2.123 \text{ W m}^{-1} \text{ K}^{-1}$), T_{bulk} is the mean temperature of the
 192 ice body within the Icestupa and l_{ice} is the average distance of any point in the surface to any other point in
 193 the ice body. T_{bulk} is initialised as 0°C and later determined from Eqn. 16 as follows:

$$T_{bulk}^{i+1} = T_{bulk} - (q_G \cdot A \cdot \Delta t) / (M_{ice} \cdot c_{ice}) \quad (17)$$

194 Since AIR's typically have conical shapes with $r_{ice} \gg h_{ice}$, we assume that the center of mass of the ice
 195 body is near the base of the fountain. Thus, the distance of every point in the AIR surface layer from the ice
 196 body's center of mass is between h_{ice} and r_{ice} . So we calculate q_G here assuming $l_{ice} = (r_{ice} + h_{ice})/2$.

197 3.3 Surface temperature

198 The available energy q_{surf} can act on the surface of the AIR to a) change its temperature, b) melt ice or
 199 c) freeze ice. So Eqn. 7 can be rewritten as:

$$q_{surf} = q_{freeze/melt} + q_T \quad (18)$$

200 where q_T , q_{freeze} and q_{melt} represent energy associated with process (a), (b) and (c) respectively.

201 To distribute the surface energy flux into these three components, we categorize the model time steps
 202 as freezing or melting events. Freezing events can only occur if there is fountain water available and the
 203 surface energy flux is negative. But just these two conditions are not sufficient as the latent heat energy
 204 can only contribute to temperature fluctuations. So to prevent latent heat energy from turning a melting
 205 event into a freezing event an additional condition namely $(q_{surf} - q_L) < 0$ is required. Thus, freezing and
 206 melting events are identified as follows:

$$q_{freeze/melt} = \begin{cases} q_{freeze} & \text{if } \Delta M_F > 0 \text{ and } q_{surf} < 0 \text{ and } (q_{surf} - q_L) < 0 \\ q_{melt} & \text{otherwise} \end{cases} \quad (19)$$

207 During a freezing event, the available energy $(q_{surf} - q_L)$ can either be sufficient or insufficient to
 208 freeze the fountain water available. If insufficient, the additional energy further cools down the surface
 209 temperature. So the surface energy flux distribution during a freezing event can be represented as:

$$(q_{freeze}, q_T) = \begin{cases} (q_{surf} - q_L, q_L) & \text{if } \Delta M_F \geq -\frac{(q_{surf} - q_L)A \cdot \Delta t}{L_f} \\ \left(\frac{\Delta M_F \cdot L_f}{A \cdot \Delta t}, q_{surf} + \frac{\Delta M_F \cdot L_f}{A \cdot \Delta t}\right) & \text{if } \Delta M_F < -\frac{(q_{surf} - q_L)A \cdot \Delta t}{L_f} \end{cases} \quad (20)$$

Table 2. Free parameters in the model categorised as constant, uncertain and site parameters. Base value (B) and uncertainty (U) were taken from the literature. For assumptions (assum.), the uncertainty was chosen to be relatively large (5 %). For measurements (meas.), the uncertainty due to parallax errors is chosen to be (1 %).

Constant Parameters	Symbol	Value	References
Van Karman constant	κ	0.4	B: Cuffey and Paterson
Stefan Boltzmann constant	σ	$5.67 \cdot 10^{-8} W m^{-2} K^{-4}$	B: Cuffey and Paterson
Air pressure at sea level	$p_{0,a}$	1013 hPa	B: Mölg and Hardy
Density of water	ρ_w	$1000 kg m^{-3}$	B: Cuffey and Paterson
Density of ice	ρ_{ice}	$917 kg m^{-3}$	B: Cuffey and Paterson
Density of air	ρ_a	$1.29 kg m^{-3}$	B: Mölg and Hardy
Specific heat of ice	c_{ice}	$2097 J kg^{-1} ^\circ C^{-1}$	B: Cuffey and Paterson
Specific heat of water	c_w	$4186 J kg^{-1} ^\circ C^{-1}$	B: Cuffey and Paterson
Specific heat of air	c_a	$1010 J kg^{-1} ^\circ C^{-1}$	B: Mölg and Hardy
Thermal conductivity of ice	k_{ice}	$2.123 W m^{-1} K^{-1}$	B: Bonales et al.
Latent Heat of Sublimation	L_s	$2848 kJ kg^{-1}$	B: Cuffey and Paterson
Latent Heat of Fusion	L_f	$334 kJ kg^{-1}$	B: Cuffey and Paterson
Uncertain Parameters		Range	
Precipitation	T_{ppt}	$1 ^\circ C$	$\pm 1 ^\circ C$
Temperature threshold			B + U: Fujita and Ageta, Zhou et al.
Ice Emissivity	ϵ_{ice}	0.95	[0.949, 0.993]
Ice Albedo	α_{ice}	0.35	$\pm 5 \%$
Snow Albedo	α_{snow}	0.85	$\pm 5 \%$
Albedo Decay Rate	τ	10 days	[1, 22] days
Surface layer thickness	Δx	20 mm	$\pm 5 \%$
Water temperature	T_{water}	$1 ^\circ C$	[0, 2] $^\circ C$
			B + U: assum.

210 During a melting event, the surface energy flux (q_{surf}) is first used to change the surface temperature to
 211 T_{temp} calculated as:

$$T_{temp} = \frac{q_{surf} \cdot \Delta t}{\rho_{ice} \cdot c_{ice} \cdot \Delta x} + T_{ice} \quad (21)$$

212 If $T_{temp} > 0^\circ C$, then energy is reallocated from q_T to q_{melt} to maintain surface temperature at melting
 213 point. So the surface energy flux distribution during a melting event can be represented as:

$$(q_{melt}, q_T) = \begin{cases} (0, q_{surf}) & \text{if } T_{temp} < 0 \\ \left(\frac{T_{temp} \cdot \rho_{ice} \cdot c_{ice} \cdot \Delta x}{\Delta t}, q_{surf} - \frac{T_{temp} \cdot \rho_{ice} \cdot c_{ice} \cdot \Delta x}{\Delta t} \right) & \text{if } T_{temp} > 0 \end{cases} \quad (22)$$

214 3.4 Mass Balance

215 The mass balance equation for an AIR is represented as:

$$\frac{\Delta M_F + \Delta M_{ppt} + \Delta M_{dep}}{\Delta t} = \frac{\Delta M_{ice} + \Delta M_{water} + \Delta M_{sub} + \Delta M_{runoff}}{\Delta t} \quad (23)$$

216 where M_F is the discharge of the fountain; M_{ppt} is the cumulative precipitation; M_{dep} is the cumulative
 217 accumulation through water vapour deposition; M_{ice} is the cumulative mass of ice; M_{water} is the cumulative
 218 mass of melt water; M_{sub} represents the cumulative water vapor loss by sublimation and M_{runoff} represents
 219 the fountain discharge runoff that did not interact with the AIR. The LHS of equation 23 represents the rate
 220 of mass input and the RHS represents the rate of mass output for an AIR.

221 Precipitation input is calculated as shown in equation 24a where ρ_w is the density of water (1000
 222 $kg\ m^{-3}$), ppt is the measured precipitation rate in [$m\ s^{-1}$] and T_{ppt} is the temperature threshold below
 223 which precipitation falls as snow. Here, snowfall events were identified using T_{ppt} as $1^{\circ}C$. Snow mass
 224 input is calculated by assuming a uniform deposition over the entire circular footprint of the Icestupa.

225 The latent heat flux is used to estimate either the evaporation and condensation processes or sublimation
 226 and deposition processes as shown in equation 24b. During time steps at which surface temperature is
 227 below $0^{\circ}C$ only sublimation and deposition can occur, but if the surface temperature reaches $0^{\circ}C$,
 228 evaporation and condensation can also occur. As the differentiation between evaporation and sublimation
 229 (and condensation and deposition) when the air temperature reaches $0^{\circ}C$ is challenging, we assume
 230 that negative (positive) latent heat fluxes correspond only to sublimation (deposition), i.e. no evaporation
 231 (condensation) is calculated.

232 Since we have categorized every time step as a freezing and melting event, we can determine the meltwater
 233 and ice generated using the associated energy fluxes as shown in equations 24c and 24d. Having calculated
 234 all the other mass components the fountain wastewater generated every time step can be calculated using
 235 equation 24e.

$$\frac{\Delta M_{ppt}}{\Delta t} = \begin{cases} \pi \cdot r_{ice}^2 \cdot \rho_w \cdot ppt & \text{if } T_a < T_{ppt} \\ 0 & \text{if } T_a \geq T_{ppt} \end{cases} \quad (24a)$$

$$\left(\frac{\Delta M_{dep}}{\Delta t}, \frac{\Delta M_{sub}}{\Delta t} \right) = \begin{cases} \frac{q_L \cdot A}{L_s} \cdot (1, 0) & \text{if } q_L \geq 0 \\ \frac{q_L \cdot A}{L_s} \cdot (0, -1) & \text{if } q_L < 0 \end{cases} \quad (24b)$$

$$\frac{\Delta M_{water}}{\Delta t} = \frac{q_{melt} \cdot A}{L_f} \quad (24c)$$

$$\frac{\Delta M_{ice}}{\Delta t} = \frac{q_{freeze} \cdot A}{L_f} + \frac{\Delta M_{ppt}}{\Delta t} + \frac{\Delta M_{dep}}{\Delta t} - \frac{\Delta M_{sub}}{\Delta t} - \frac{\Delta M_{melt}}{\Delta t} \quad (24d)$$

$$\frac{\Delta M_{runoff}}{\Delta t} = \frac{\Delta M_F - \Delta M_{ice}}{\Delta t} \quad (24e)$$

236 To estimate the mass of any component at time step i , one can now sum the mass flux estimated above:

$$M_{comp}^i = \sum_{t=0}^{t=i} \left(\frac{\Delta M_{comp}}{\Delta t} \right)_t + M_{comp}^0 \quad (25)$$

237 where

$$M_{comp}^0 = \begin{cases} -V_{dome} * \rho_{ice} & \text{if } M_{comp} = M_{ice} \text{ or } M_F \\ 0 & \text{otherwise} \end{cases} \quad (26)$$

238 Considering AIRs as water reservoirs, we can quantify their potential through the amount of water they
 239 store (storage quantity) and the length of time they store it (storage duration). Another means of comparing
 240 different Icestupas is through their water storage efficiency defined accordingly as:

$$\text{Storage Efficiency} = \frac{M_{water}}{(M_F + M_{ppt} + M_{dep})} \cdot 100 \quad (27)$$

4 MODEL RESULTS

241 The model was forced with meteorological data from 22nd November to 10th May 2021 (Fig. 3) and
 242 various parameters (see Table 2) to calculate the mass and energy balance of the CH21 AIR.

243 4.1 Energy and mass balance calculation

244 Daily averages of some components of the energy balance are shown in Fig. 6 (b). On average during
 245 the experiment duration, the total energy balance was almost zero. Net shortwave radiation (35 W m^{-2}),
 246 sensible (41 W m^{-2}) and latent heat flux (2 W m^{-2}) with a mostly positive flux towards the surface of the
 247 icestupa were compensated by the net longwave radiation (- 47 W m^{-2}), the fountain water heat flux (-
 248 13 W m^{-2}) and the freeze/melt energy (- 19 W m^{-2}). The contributions of other fluxes were negligible in
 249 comparison.

250 Net shortwave radiation is the main input to, and the most varying energy flux on the ice surface. Its
 251 variability is controlled by the surface albedo α and the area fraction f_{cone} which therefore represent key
 252 variables in the energy balance (Fig. 7 (b)). Although global radiation flux reached a daily maximum value
 253 of 340 W m^{-2} , q_{SW} only went up to 114 W m^{-2} . This is caused by the fact that less than 40 % of the direct
 254 solar radiation influenced the Icestupa surface as shown by the area fraction f_{cone} in Fig. 7 (a). Snowfall is
 255 the atmospheric variable connected most closely and proportionally to albedo. Higher and/or more frequent
 256 snowfall thus decreases the energy available for melt due to the corresponding increase in α .

257 q_{LW} was predominantly negative indicating that this energy balance component drove the freezing of
 258 the ice structure. Daily values of q_{LW} ranged from -101 to 19 W m^{-2} . Turbulent sensible heat flux q_S
 259 contributed mostly to the melt of the ice structure. Daily values of q_S ranged from -3 to 410 W m^{-2} . Daily
 260 values of the turbulent latent heat flux q_L ranged from -90 to 157 W m^{-2} . Since the mean of q_L was positive,
 261 the Icestupa gained mass cumulatively from the atmosphere due to the deposition process. Daily values
 262 of fountain water heat flux ranged from -119 to 4 W m^{-2} . q_F was also a significant contributor to the
 263 freezing process like q_{LW} . So the influence of the fountain on the energy balance and the freezing events
 264 was significant. The contribution of heat flux by conduction q_G was minimal as it only varied between
 265 -1 to 3 W m^{-2} with a mean of 0 W m^{-2} . The energy contributing to surface temperature changes (q_T)
 266 was insignificant in comparison to the energy spent on freezing and melting ($q_{freeze/melt}$). The resulting
 267 bulk temperature and the surface temperature are shown in Fig. 7 (b). For the total considered period,
 268 $q_{freeze/melt}$ accounted for 30% of overall energy turnover. The energy turnover is calculated as the sum of
 269 energy fluxes in absolute values. q_{LW} accounted for 22%, followed by q_S (20%), q_{SW} (16%), q_L (5%), q_F
 270 (6%), q_T (1%) and q_G (0%).

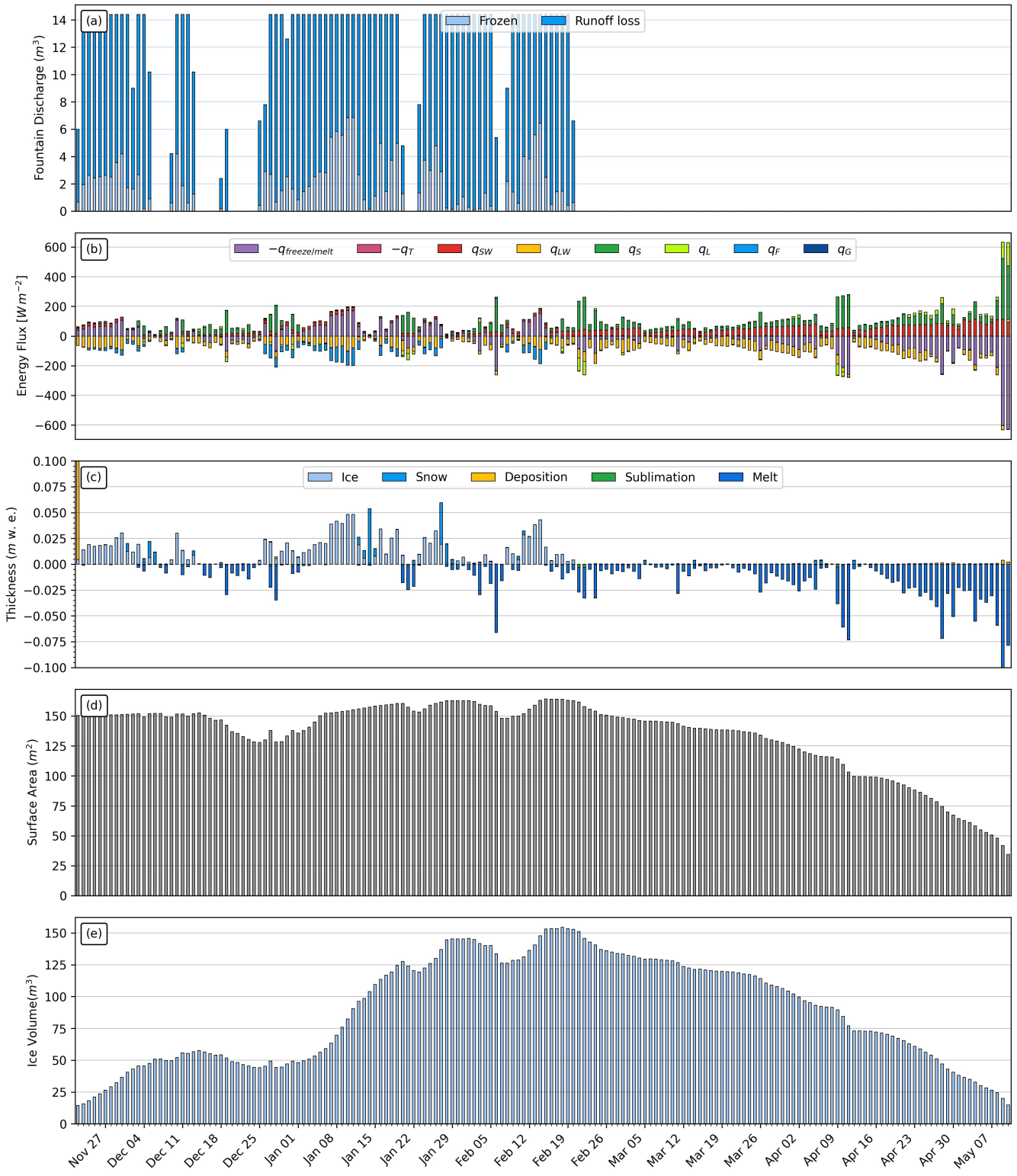


Figure 6. (a) Fountain discharge (b) energy flux components, (c) mass flux components (d) surface area and (e) volume of the Icestupa in daily time steps. q_{SW} is the net shortwave radiation; q_{LW} is the net longwave radiation; q_L and q_S are the turbulent latent and sensible heat fluxes. q_F represents the interactions of the fountain water with the AIR surface layer. q_G quantifies the heat conduction process between the AIR surface layer and the ice body.

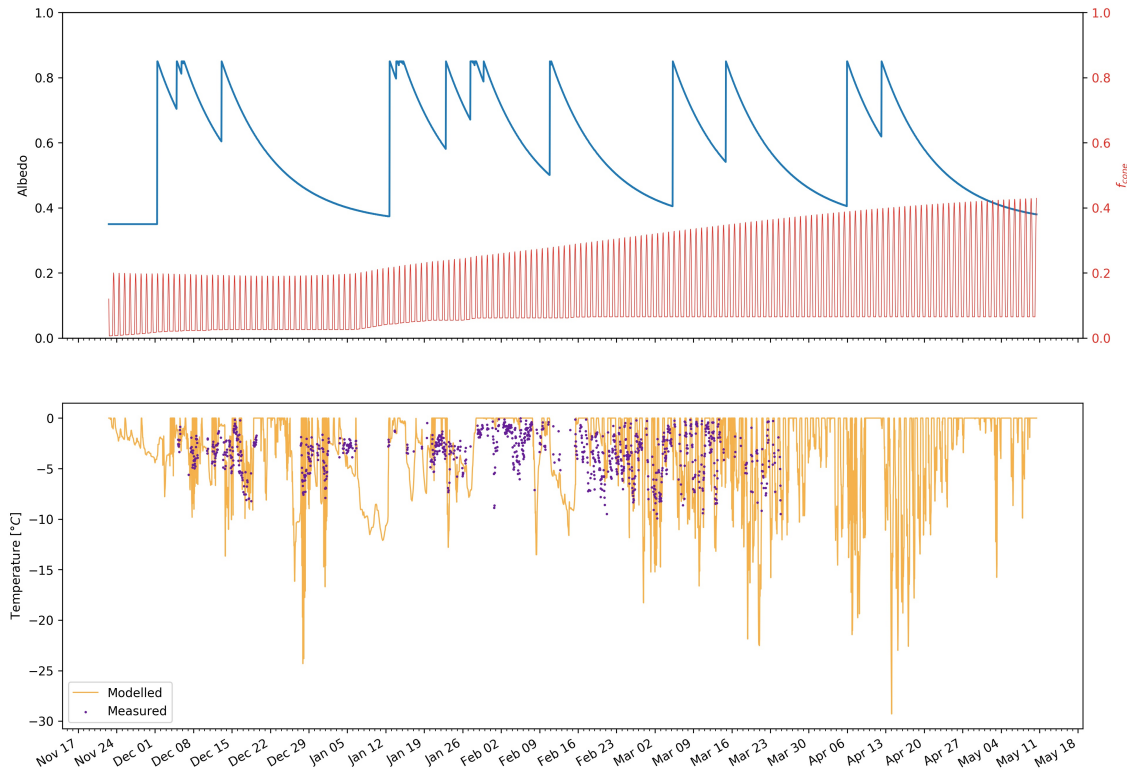


Figure 7. Some derived parameters of the model, namely, albedo and f_{cone} (a), Surface and bulk temperature (b). In (a), the green curve shows how snow and fountain-on events reset albedo between ice albedo and snow albedo. The decay of the snow albedo to ice albedo can also be observed. The orange curve shows how the solar radiation area fraction varied diurnally with variations in the solar elevation angle. In (b), the surface temperature (light blue curve) was forced to be 0°C during fountain activity. The corresponding bulk temperature is shown with the dark blue curve.

Table 3. Summary of mass balance components for the CH21 AIR at the end of the model run on 10th May 2021.

	Component	CH21
Input	M_F	987,918
	M_{ppt}	29,533
	M_{dep}	4,755
Output	M_{water}	196,011
	M_{ice}	182
	M_{sub}	4,747
	M_{runoff}	821,267

271 Fig. 6 (c) represents the mass fluxes associated with these energy exchanges expressed in m w.e. It shows
 272 the ice and meltwater formed due to q_{melt} , snow accumulated due to precipitation, water vapour deposition
 273 and sublimation due to q_L .

274 The total water used for the Icestupa development includes contributions from the fountain (96.7%),
 275 snowfall (2.9 %), deposition (0.5 %) as shown in Table 3. Therefore, in the case of CH21 we used a water
 276 input of 1,034,328 kg, with a resultant storage efficiency of 19 %.

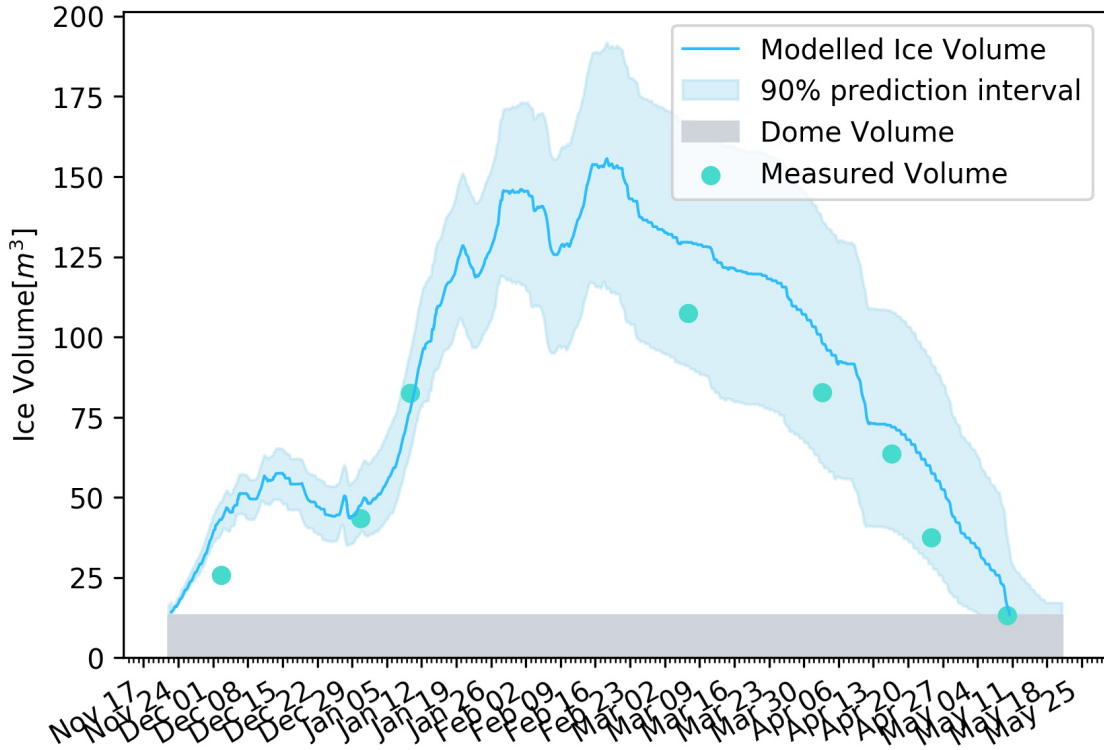


Figure 8. Modelled ice volume during the lifetime of the CH21 AIR (blue curve). Green points indicate the validation measurements. The prediction interval is based on the ice volume uncertainty caused by the most sensitive parameters, namely, temperature threshold below which precipitation falls as snow and the ice emissivity.

5 MODEL SENSITIVITY AND UNCERTAINTY ANALYSIS

277 The icestupa model can be regarded as a function $f(x_1, x_2 \dots, x_n) = (y_1, y_2 \dots, y_m)$, where
 278 $(x_1, x_2 \dots, x_n)$ are the model parameters and $(y_1, y_2 \dots, y_m)$ are the model outputs. The influence of each
 279 parameter on the output variables of interest were quantified and the most important physical parameters
 280 for the subsequent uncertainty analysis were determined. The sensitivity of a parameter x_j is determined
 281 by keeping all other parameters $x_i, i \neq j$ fixed at their baseline value and varying x_j within values that are
 282 physically plausible.

283 A sensitivity study on the parameters (listed in Table 2) was performed with the maximum ice volume
 284 as the target variable. All the parameters were assumed to be independent of each other with a uniform
 285 distribution. This assumption ignores the auto-correlation present among the parameters associated with
 286 the albedo parameterisation. The range of uncertain parameters were set based on available literature values
 287 or varied $\pm 5\%$ from the base value if no such reference was available. The uncertainty of all the site
 288 parameters were caused due to parallax errors during manual measurement. This was quantified with a
 289 range of $\pm 1\%$ from the base value. However, it must be kept in mind that, even though intended to be as
 290 objective as possible, the selection of a parameter range has a subjective part that influences the results and
 291 conclusions obtained in this analysis. The variation of the model outputs y_k is evaluated to quantify the
 292 local sensitivities $s_{j,k}$ that are defined here as the 95% range of the simulated outputs.

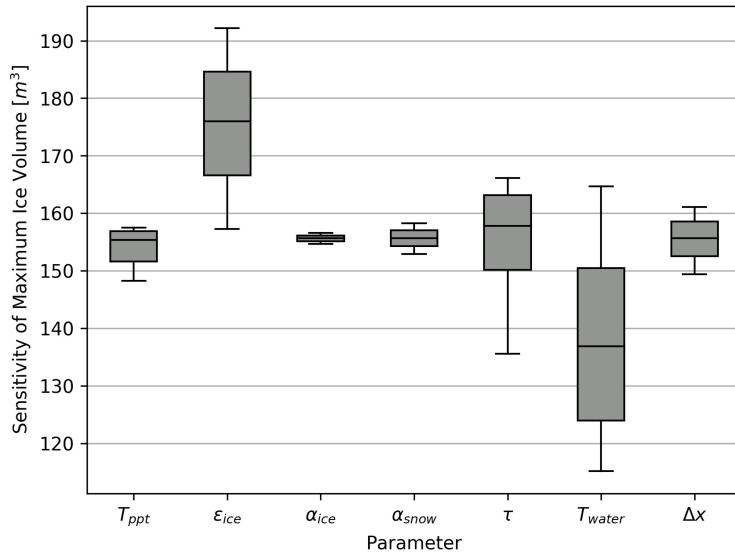


Figure 9. Sensitivities of maximum ice volume to all the uncertain and site parameters used in the model (Table 2).

293 To perform the uncertainty analysis, we included only parameters that influence the maximum ice volume
 294 by at least 0.1m^3 . All other parameters were fixed at their baseline value. Fig. 9 shows all the variance
 295 produced by these uncertain parameters in maximum ice volume calculation.

296 In total, the sensitivity analysis required 120 simulations, and the uncertainty analysis a total of 662
 297 simulations.

6 DISCUSSION

298 6.1 Important assumptions

299 In the sensitivity and uncertainty analysis presented above, we did not account for several general
 300 assumptions and parametrisation choices that may cause model errors. Some assumptions and their
 301 potential to cause errors are discussed below.

- 302 • Turbulent Sensible and Latent Heat Fluxes: The method used to calculate the turbulent heat fluxes
 303 by Garratt (1992) assumes that the turbulent heat fluxes are acting over a uniform planar surface to
 304 determine the roughness length. Since our application is on a conical surface, the distance to the ice
 305 surface is not uniform and well defined. Hence, z_{ice} has no real physical significance here.
- 306 • Droplet flight time loss: Water losses during the flight time of fountain droplets were neglected making
 307 all the fountain spray available for freezing. For the CH21 experiment, inclusion of this parameter does
 308 not influence results since it is already accounted for in the runoff water discharge rate which was at
 309 least 3l min^{-1} .
- 310 • Nucleation of droplets: Corresponding to droplet flight time, ice/snow formation is also possible before
 311 surface contact if nucleation occurs during flight time. For the CH21 experiment, this process will
 312 further increase the freeze rate and hence the storage efficiency. This process is neglected for model
 313 simplicity.
- 314 • Shape Effects: The suppression of heat exchange between the snow/ice surface and the air adjacent
 315 to the surface effectively slows down snow/ice ablation in spring and promotes the stagnation of the

Table 4. AIR Results

AIR	IN21	CH21	CH20	CH19
Max Ice Volume [m^3]	703	156	107	1
Storage Efficiency [%]	18	19	14	3
Storage Duration [days]	?	169	93	45
Validation RMSE [m^3]	59	13	25	0.2

316 cold air within topographical depressions (Fujita et al., 2010). The quantitative contribution of the
 317 atmospheric decoupling over melting snow/ice for the total mass and energy balance is ignored in the
 318 model.

7 CONCLUSIONS

319 We outlined a methodology for estimating ice, liquid water, water vapour and runoff quantities produced
 320 during the construction of an AIR using measurements of fountain spray rate, air temperature, radiation,
 321 humidity, pressure, wind and cloudiness at four different study sites. The comparison with all the validation
 322 measurements at two different dates during the experiment led to satisfying results as shown in Table 4.

323 The model results support the hypothesis that there could be considerable water loss during the formation
 324 of AIR particularly due to excessive fountain spray. Further experiments at different locations with different
 325 fountains are required to better understand the influence of construction decisions on the results.

8 APPENDIX

8.1 Ladakh Icestupa 2014/15

327 A 20 m tall Icestupa (Wangchuk, 2015c) was built in Phyang village, Ladakh at an altitude of 3500
 328 m a.s.l. Assuming a conical shape with a diameter of 20 m, the corresponding volume of this Icestupa
 329 becomes 2093 m^3 or 1,920 m^3 w.e. The fountain sprayed water at a rate of 210 l min^{-1} (Wangchuk,
 330 2015e) from 21st January (Wangchuk, 2015a) to at least until 5th March 2015 (Wangchuk, 2015b) (around
 331 43 nights). Assuming fountain spray was active for 8 hours each night, we estimate water consumption to
 332 be around 4,334 m^3 . Thus, during the construction/freezing period of the Icestupa, roughly 56 % of the
 333 water provided was wasted. The actual water loss is bound to be much higher due to further vapour losses
 334 during the melting period. This Icestupa completely melted away on 6th July 2015 (Wangchuk, 2015d).
 335 Therefore, the storage duration was 166 days or roughly 5 months.

8.2 CH19 AIR

337 The CH19 AIR in the Schwarzsee region lies at 967 m a.s.l.. In the winter (Oct-Apr), mean daily
 338 maximum and minimum air temperatures vary between -4 and 14 °C. Clear skies are rare, averaging
 339 around 7 days, and precipitation amounts average 155 mm per month during winter (Meteoblue, 2020).
 340 The site was situated adjacent to a stream resulting in high humidity values across the study period. Within
 341 the EP site, an enclosure with a 1.8 m radius was constructed for the experiment. An automatic weather
 342 station (AWS) was adjacent to the wooden boundary as shown in Fig. ???. The fountain used for spraying
 343 water had a nozzle diameter of 5 mm and a height of 1.35 m, and was placed in the centre of the wooden
 344 enclosure. The water was transferred from a spring water source at 1267 m a.s.l. by pipeline and flowed
 345 via a flowmeter and an air escape valve to the nozzle, where it was sprinkled with a spray radius of around
 346 1.7 m. The air escape valve was installed to avoid errors in the flow measurements due to air bubbles. In
 347 addition, a webcam guaranteed a continuous survey of the site during the construction of the Icestupa.

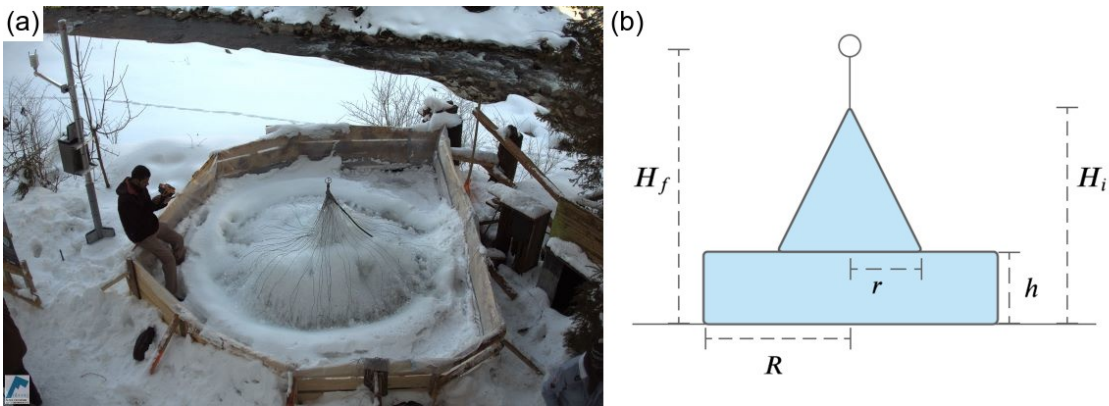


Figure 10. (a) The ice structure during the first validation measurement as seen on the webcam image of 14th Feb. (b) The corresponding cross section of the EP ice structure with the field estimates of r , R , h , H_i , H_f used to determine the Icestupa volume is shown on the right.

348 8.2.1 Weather data

349 Precipitation data was derived from the Plaffeien AWS (IDAWEB, 2019) located 8.8 km away from
 350 the measurement site at an altitude of 1042 m a.s.l. We recognised during our data analysis that, except
 351 precipitation, all the other meteorological variables of the EP site correlated much better with the ERA5
 352 dataset than the nearby Plaffeien AWS dataset. The 2 m temperature parameter correlated with air
 353 temperature ($r^2 = 0.9$), surface pressure parameter correlated with air pressure ($r^2 = 1$) and 10m
 354 wind speed parameter (derived from horizontal and vertical components) correlated with wind speed
 355 ($r^2 = 0.6$).

356 Due to a power failure, all data from the EP AWS was lost from 27th February 15:20 2019 to 2nd March
 357 15:00 2019 (equivalent to around 7% of the measurement period). During heavy snowfall events, the
 358 ultrasonic wind sensor was blocked and recorded zero values. ERA5 was used to fill such errors and data
 359 gaps.

360 The ERA5 grid point chosen (Latitude 46° 38' 24" N, Longitude 7° 14' 24" E) for the EP site was around
 361 9 km away from the actual site. Near-surface humidity is not provided directly in ERA5 dataset, but from
 362 near-surface (2 m from the surface) temperature (T_{ERA5}) and dew point temperature (Tw_{ERA5}) the relative
 363 humidity (RH) at 2 m was calculated as:

$$RH = 100 \cdot \frac{e_{sat}(Tw_{ERA5})}{e_{sat}(T_{ERA5})} \quad (28)$$

364 where the saturation vapour pressure function e_{sat} is expressed with the Teten's formula (Tetens, 1930):

$$e_{sat}(T) = a_1 \cdot e^{(a_3 \cdot \frac{T}{(T+273.16-a_4)})} \quad (29)$$

365 with T in °C and the parameters set for saturation over water ($a_1 = 611.21$ Pa, $a_3 = 17.502$ and $a_4 = 32.19$
 366 K) according to Buck (1981).

367 All the ERA5 variables were therefore fitted with the EP dataset via linear regressions. With the modified
 368 ERA5 dataset, we were also able to further extend the EP dataset and allow the model to run beyond 18th
 369 March 2019. Precipitation was filled as null values beyond 18th March 2019.

370 8.2.2 Fountain spray radius of CH19 AIR

371 This fountain spray radius is determined by modelling the projectile motion of the water droplets. Using
 372 mass conservation, the droplet speed v_F can be determined from the spray rate d_F and the diameter dia_F
 373 of the nozzle as follows:

$$v_F = \frac{d_F}{\pi \cdot dia_F^2 / 4} \quad (30)$$

374 Afterwards, we assume that the water droplets move with an air friction free projectile motion from
 375 the fountain nozzle with a height h_F to the ice/ground surface. The resulting spray radius r_F was then
 376 determined from the projectile motion equation as follows:

$$r_F = \frac{v_F \cdot \cos\theta_F (v_F \cdot \sin\theta_F + \sqrt{(v_F \cdot \sin\theta_F)^2 + 2 \cdot g \cdot h_F})}{g} \quad (31)$$

377 where $g = 9.8 \text{ ms}^{-2}$ is the acceleration due to gravity and $\theta_F = 45^\circ$ is the angle of launch.

378 8.2.3 CH19 Field Measurements for validation

379 The volume was determined by decomposing the ice structure into a cylinder (length $2R$ and height h)
 380 and a cone (radius r and height $(H_i - h)$) through the following equation:

$$V = \pi \cdot R^2 \cdot h + 1/3 \cdot \pi \cdot r^2 \cdot (H_i - h) \quad (32)$$

381 Manual measurements were performed at the end of the freezing period on 14th February 16:00 2019
 382 (only one more fountain run was possible after this date) to estimate r, R, h, H_i, H_f (see Fig. ?? for the
 383 different geometry components):

$$0.55 \leq r \leq 1m ; 1.1 \leq R \leq 1.2m ; 0.1 \leq h \leq 0.2m ; 0.6 \leq H_i \leq 0.8m ; 1.3 \leq H_f \leq 1.4m$$

384 The ranges of the variables show the variance of the Icestupa's dimensions across different compass
 385 orientations. Correspondingly, the volume range estimated for the first validation point was 0.857 ± 0.186
 386 m^3 on 14th February 16:00 2019.

387 The second validation point corresponds to the end of the melting process on 10th March 18:00 2019.
 388 Based on the webcam imagery and manual measurement, a thin layer of ice with an observed thickness
 389 between 0.01 to 0.06 m could be quantified. This results in the volume range for the second validation to
 390 be $0.13 \pm 0.09 \text{ m}^3$ on 11th March 2019

391 In reality, the EP ice structure was more cylindrical until a height of 0.2 m and conical afterwards until a
 392 height of 0.6 m with a radius of 1.18 m. However, we assume a conical shape of this ice structure in order
 393 to apply the modelling strategy described below.

394 8.2.4 CH21 and CH20 Surface temperature corrections

395 We discarded some thermal camera temperature measurements due to the following reasons:

- 396 • Snowfall/fog: Whenever there was snow or thick fog, the thermal image was corrupted. Refer image
397 Jan14 1900 and Jan3 800. We used the standard deviation of the pixel temperature to identify these
398 events and remove them from the validation dataset.
- 399 • Strong sunlight: Usually at noon, especially in end of Feb and March, we observed that ice temperature
400 values were above zero C. We found that again the thermal cam images were corrupted as seen in
401 Mar6 1300. So we removed all temperature values above 0 C.
- 402 • Then there were some images that were completely blue and looked corrupted. We cannot identify the
403 cause here but I filtered them out using the mean of all temperature pixels.

REFERENCES

- 404 Apel, H., Abdykerimova, Z., Agalhanova, M., Baimaganbetov, A., Gavrilko, N., Gerlitz, L., et al. (2018).
405 Statistical forecast of seasonal discharge in central asia using observational records: development of a
406 generic linear modelling tool for operational water resource management. *Hydrology and Earth System
407 Sciences* 22, 2225–2254. doi:10.5194/hess-22-2225-2018
- 408 Bonales, L. J., Rodriguez, A. C., and Sanz, P. D. (2017). Thermal conductivity of ice prepared under
409 different conditions. *International Journal of Food Properties* 20, 610–619. doi:10.1080/10942912.
410 2017.1306551
- 411 Buck, A. L. (1981). New equations for computing vapor pressure and enhancement factor. *Journal of
412 Applied Meteorology and Climatology* 20, 1527 – 1532
- 413 Buytaert, W., Moulds, S., Acosta, L., Bievre, B. D., Olmos, C., Villacis, M., et al. (2017). Glacial melt
414 content of water use in the tropical andes. *Environmental Research Letters* 12, 114014. doi:10.1088/
415 1748-9326/aa926c
- 416 Chen, Y., Li, W., Deng, H., Fang, G., and Li, Z. (2016). Changes in central asia's water tower: Past, present
417 and future. *Nature* doi:10.1088/1748-9326/aa926c
- 418 [Dataset] Copernicus Climate Change Service (C3S) (2017). Era5: Fifth generation ecmwf atmospheric
419 reanalyses of the global climate. [Available at [https://cds.climate.copernicus.eu/
420 cdsapp#!/home](https://cds.climate.copernicus.eu/cdsapp#!/home), accessed 2019-10-01]
- 421 Cuffey, K. M. and Paterson, W. S. B. (2010). *The Physics Of Glaciers* (Elsevier)
- 422 Fujita, K. and Ageta, Y. (2000). Effect of summer accumulation on glacier mass balance on the
423 tibetan plateau revealed by mass-balance model. *Journal of Glaciology* 46, 244–252. doi:10.3189/
424 172756500781832945
- 425 Fujita, K., Hiyama, K., Iida, H., and Ageta, Y. (2010). Self-regulated fluctuations in the ablation of a snow
426 patch over four decades. *Water Resources Research* 46, W11541. doi:10.1029/2009WR008383
- 427 Garratt, J. R. (1992). *The Atmospheric Boundary Layer* (Cambridge University Press)
- 428 Grossman, D. (2015). As himalayan glaciers melt, two towns face the fallout [Available at
429 [https://e360.yale.edu/features/as_himalayan_glaciers_melt_two_towns_
430 face_the_fallout](https://e360.yale.edu/features/as_himalayan_glaciers_melt_two_towns_face_the_fallout), accessed 2019-10-01]
- 431 Hock, R. (2005). Glacier melt: a review of processes and their modelling. *Progress in Physical Geography:
432 Earth and Environment* 29, 362–391
- 433 Hock, R., Rasul, G., Adler, C., Cáceres, B., Gruber, S., Hirabayashi, Y., et al. (2019). 2019: High mountain
434 areas. *IPCC Special Report on the Ocean and Cryosphere in a Changing Climate* [H.-O. Pörtner, D.C.
435 Roberts, V. Masson-Delmotte, P. Zhai, M. Tignor, E. Poloczanska, K. Mintenbeck, A. Alegria, M. Nicolai,
436 A. Okem, J. Petzold, B. Rama, N.M. Weyer (eds.)]
- 437 Hoelzle, M., Barandun, M., Bolch, T., Fiddes, J., Gafurov, A., Muccione, V., et al. (2019). *The status and
438 role of the alpine cryosphere in Central Asia*. doi:10.4324/9780429436475-8

- 439 Hori, M., Aoki, T., Tanikawa, T., Motoyoshi, H., Hachikubo, A., Sugiura, K., et al. (2006). In-situ
440 measured spectral directional emissivity of snow and ice in the 8–14 micrometer atmospheric window.
441 *Remote Sensing of Environment* 100, 486 – 502
- 442 [Dataset] IDAWEB (2019). Meteoswiss, federal office of meteorology and climatology. [Available at
443 <https://gate.meteoswiss.ch/idaweb/login.do>, accessed 2019-10-01]
- 444 Immerzeel, W. W., Lutz, A. F., Andrade, M., Bahl, A., Biemans, H., Bolch, T., et al. (2019). Importance
445 and vulnerability of the world's water towers. *Nature* 577, 364 – 369. doi:10.1038/s41586-019-1822-y
- 446 Meteoblue (2020). Climate schwarzsee [Available at https://www.meteoblue.com/en/weather/historyclimate/climatemodeled/schwarzsee_switzerland_11790334, accessed 2019-10-01]
- 447 Mölg, T. and Hardy, D. R. (2004). Ablation and associated energy balance of a horizontal glacier surface
448 on kilimanjaro. *J. Geophys. Res.-Atmos.* 109, 1–13. doi:10.1029/2003JD004338
- 449 Nüsser, M., Dame, J., Kraus, B., Baghel, R., and Schmidt, S. (2019a). Socio-hydrology of artificial glaciers
450 in ladakh, india: assessing adaptive strategies in a changing cryosphere. *Regional Environmental Change*
451 doi:10.1007/s10113-018-1372-0
- 452 Nüsser, M., Dame, J., Parveen, S., Kraus, B., Baghel, R., and Schmidt, S. (2019b). Cryosphere-Fed
453 Irrigation Networks in the Northwestern Himalaya: Precarious Livelihoods and Adaptation Strategies
454 Under the Impact of Climate Change. *Mountain Research and Development* 39. doi:10.1659/
455 MRD-JOURNAL-D-18-00072.1
- 456 Oerlemans, J. and Knap, W. H. (1998). A 1 year record of global radiation and albedo in the
457 ablation zone of morteratschgletscher, switzerland. *Journal of Glaciology* 44, 231–238. doi:10.
3189/S0022143000002574
- 458 Scherrer, S. C. (2020). Temperature monitoring in mountain regions using reanalyses: lessons from the
459 alps. *Environmental Research Letters* 15, 044005
- 460 Schmidt, L. S., Aðalgeirs ðóttir, G., Guðmundsson, S., Langen, P. L., Pálsson, F., Mottram, R., et al. (2017).
461 The importance of accurate glacier albedo for estimates of surface mass balance on vatnajökull: evaluating
462 the surface energy budget in a regional climate model with automatic weather station observations. *The
463 Cryosphere* 11, 1665–1684. doi:10.5194/tc-11-1665-2017
- 464 Tetens, O. (1930). Über einige meteorologische begriffe. z. *Geophys.* 6, 297–309
- 465 Unger-Shayesteh, K., Vorogushyn, S., Farinotti, D., Gafurov, A., Duethmann, D., Mandychev, A., et al.
466 (2013). What do we know about past changes in the water cycle of central asian headwaters? a review.
467 *Global and Planetary Change* 110, 4 – 25. doi:10.1016/j.gloplacha.2013.02.004. Water in Central Asia
468 – Perspectives under global change
- 469 Wangchuk, S. (2014). Ice stupa artificial glaciers of ladakh [Available at www.indiegogo.com/projects/ice-stupa-artificial-glaciers-of-ladakh#/, accessed 2019-10-01]
- 470 Wangchuk, S. (2015a). The good news at ice stupa 24th january 2015 [Available at <http://icestupa.org/news/the-good-news-at-ice-stupa>, accessed 2019-10-01]
- 471 Wangchuk, S. (2015b). Ice stupa artificial glacier inaugurated
472 5th of march 2015 [Available at <http://icestupa.org/news/ice-stupa-artificial-glacier-inaugurated-5th-of-march>, accessed
473 2019-10-01]
- 474 Wangchuk, S. (2015c). Ice stupa surpasses guiness world record [Available at <http://icestupa.org/news/ice-stupa-surpasses-guinness-world-record>, accessed 2019-10-01]
- 475 Wangchuk, S. (2015d). Ice stupa way of celebrating a special day [Available at <http://icestupa.org/news/ice-stupa-way-of-celebrating-a-special-day6th-of-ju>, accessed
476 2019-10-01]

- 484 2019-10-01]
- 485 Wangchuk, S. (2015e). World water day at ice stupa [Available at <http://icestupa.org/news/world-water-day-at-ice-stupa>, accessed 2019-10-01]
- 486
- 487 WMO (2018). *Guide to Instruments and Methods of Observation* (World Meteorological Organization ;
- 488 2018 (2018 Edition))
- 489 Woolf, H. M. (1968). *On the Computation of Solar Elevation Angles and the determination of sunrise and*
- 490 *sunset times* (National Aeronautics and Space Administration)
- 491 Zhou, S., Kang, S., Gao, T., and Zhang, G. (2010). Response of zhadang glacier runoff in nam co basin,
- 492 tibet, to changes in air temperature and precipitation form. *Chinese Science Bulletin* 55, 2103–2110.
- 493 doi:10.1007/s11434-010-3290-5